Nanoscale

PAPER

View Article Online
View Journal | View Issue

Cite this: *Nanoscale*, 2024, **16**, 5215

Unraveling a volcanic relationship of Co/N/C@Pt$_x$Co catalysts toward oxygen electro-reduction†

Yangdong Zhou,[a] Junda Chen,[a] Zhiyin Huang,[a] Yuqin Peng,[a] Lixin Xing,[a] Chunmei Tang,[a] Ning Wang,[a] Ling Meng,[a] Mingjie Wu,*[b] Lei Du *[a] and Siyu Ye*[a,c]

Received 29th December 2023,
Accepted 30th January 2024

DOI: 10.1039/d3nr06647a

rsc.li/nanoscale

The cathodic oxygen reduction reaction (ORR) has been continuously attracting worldwide interest due to the increasing popularity of proton exchange membrane (PEM) fuel cells. So far, various Pt-group metal (PGM) or PGM-free catalysts have been developed to facilitate the ORR. However, there is still a gap to achieve the expected goals as proposed by the U.S. Department of Energy (DoE). Recently, PGM-free@PGM hybrid catalysts, such as the M/N/C@PtM catalyst, have achieved the milestones of oxygen reduction, as reviewed in our recent work. It is, nevertheless, still challenging to unravel the underlying structure–property relationships. Here, by applying different Pt/Co ratios, a series of Co/N/C@Pt$_x$Co catalysts are synthesized. Interestingly, the ORR activity and stability are not linear with the Pt content, but show a volcano-like curve with increased Pt usage. This relationship has been deeply unraveled to be closely related to the contents of pyrrolic N, pyridinic N, and graphitized carbon in catalysts. This work provides guidelines to rationally design the coupled PGM-free@PGM catalysts toward the ORR by appropriate surface engineering.

Introduction

A proton exchange membrane fuel cell (PEMFC) is a clean energy generation technology that consumes oxygen and hydrogen as fuel. The PEMFC has attracted increasing attention due to its environmentally friendly and pollutant-free features. However, one of the most challenging barriers impeding commercialization and development of PEMFCs is the high Pt usage at the cathode where the sluggish oxygen reduction reaction (ORR) takes place.[1–4] As a result, it is essential to develop advanced catalysts for the ORR that have good catalytic activity, high stability, and low cost.

There are now two mature approaches for reducing Pt usage. A widely accepted way is the development of PtM alloys supported with carbon, *e.g.*, a C@PtCo catalyst applied in Toyota's Mirai vehicles,[5] which is effective in the development of Pt-group metal (PGM) catalysts at this stage. The M element is typically a transition metal, *e.g.*, Fe, Co, Ni, *etc.* By regulating the crystal structure and stoichiometry, the occupation of specific sites by Pt or M atoms can be well optimized and will lead to significant ligand and/or strain effects to enhance the intrinsic ORR activity on Pt sites.[6,7] However, the PGM catalysts still suffer from a huge resistance of local oxygen transport, a great barrier to improve the fuel cell performance.[8–24]

On the other hand, PGM-free catalysts represented by M/N/C have been emerging recently, which can avoid using the precious metal Pt. However, there is still an order-of-magnitude gap between the ORR activity of PGM-free (A $g_{catalyst}^{-1}$) and PGM catalysts (A mg_{Pt}^{-1}), and the PGM-free catalysts usually decay rapidly in the first 10 hours of operation.[24,25]

Based on the above facts, the development of both PGM-free and PGM catalysts cannot meet the requirements of PEMFC deployment. Recently, coupled PGM-free@PGM catalysts have been reported, which involve both M/N/C and PtM alloy nanoparticles.[26–36] Attractively, as far as we know, the highest reported ORR activity (2.48 A mg_{Pt}^{-1}@0.9 V[37]) and stability (97% activity retention after 100 000 cycles[32]) in PEMFC membrane electrode assemblies are based on this coupled catalyst.

At present, the coupled PGM-free@PGM catalysts need further optimization, *e.g.*, the Pt/Co ratio, while the structure-property relationship has not been well understood.[38,39] To move forward, a series of Co/N/C@Pt$_x$Co catalysts using different Pt contents are herein synthesized. It is unraveled that the Pt/Co ratio not only affects the size and uniformity of PtCo nanoparticles but also tunes the coordination structure

[a]*Huangpu Hydrogen Energy Innovation Centre/School of Chemistry and Chemical Engineering, Guangzhou University, Wai Huan Xi Road 230, Guangzhou 510006, P. R. China. E-mail: siyu.ye@gzhu.edu.cn, lei.du@gzhu.edu.cn*
[b]*State Key Laboratory of New Textile Materials and Advanced Processing Technologies, Wuhan Textile University, Wuhan 430200, P. R. China. E-mail: mjwu@wtu.edu.cn*
[c]*SinoHykey Technology Company Ltd., 8 Hongyuan Road, Huangpu District, Guangzhou 510760, P. R. China*

† Electronic supplementary information (ESI) available. See DOI: https://doi.org/10.1039/d3nr06647a

of N dopants. Interestingly, the results demonstrate a volcano-shaped relationship between the Pt/Co ratio with ORR activity and stability (activity loss) in Co/N/C@Pt$_x$Co catalysts, which is attributed to the contents of pyrrolic N, pyridinic N, and graphitized carbon. These findings might be helpful for the development of novel coupled catalysts.

Experimental details

Chemicals

Zinc nitrate hexahydrate ($Zn(NO_3)_2{\cdot}xH_2O$), cobalt nitrate hexahydrate ($Co(NO_3)_2{\cdot}6H_2O$), 2-methylimidazole (2-MeIm), methanol, chloroplatinic acid hexahydrate ($H_2PtCl_6{\cdot}6H_2O$), isopropanol, formic acid (HCOOH) and perchloric acid ($HClO_4$) were purchased from Aladdin. Nafion (5 wt%) was purchased from Dupon. Commercial Pt/C (20 wt%) was purchased from TKK (TANAKA). Distilled deionized water (18.25 MΩ cm) applied in all experiments was obtained through an ultra-pure water system in lab. All chemicals were employed without further purification.

Materials synthesis

Co/N/C substrate. The Co/N/C material as the substrate was synthesized and optimized by following our recent publication.[40] Briefly, 100 mL methanol containing 8 mM $Co(NO_3)_2{\cdot}6H_2O$ and 8 mM $Zn(NO_3)_2{\cdot}xH_2O$ was mixed with another 100 mL solution involving 32 mM 2-MeIm in methanol under vigorous agitation, followed by stirring for 8 hours. After the completion of the reaction, the obtained light pink powder was collected, washed and centrifuged. The centrifugation rate was set as 10 000 rpm and centrifugation lasted for 10 minutes, which was repeated 5 times to remove all the impurities. The obtained wet sample was then dried at 60 °C overnight, and then finely ground to prepare a Co-doped ZIF (zeolitic imidazolate framework)-8 precursor. The precursor was then pyrolyzed at 1000 °C for 3 hours under an inert N_2 atmosphere. The obtained black powder was denoted as Co/N/C.

Co/N/C@Pt$_x$Co catalyst. The "x" in Co/N/C@Pt$_x$Co represents the real molar ratio of Pt to Co. In a typical synthesis of the Co/N/C@Pt$_{0.14}$Co catalyst, 50 mg of Co/N/C was dispersed in 50 mL ultrapure water (18.25 MΩ cm) followed by the addition of 26 μL H_2PtCl_6 (0.09663 M), *i.e.*, 0.00256 mM or 0.5 mg of Pt element. Then, 1 mL HCOOH was added to the suspension under vigorous stirring at 80 °C for 10–12 h to reduce H_2PtCl_6. The black precursor sample was collected and washed by vacuum filtration, before vacuum drying at 60 °C overnight. The precursor was then placed in a tube furnace for further pyrolysis, which was performed at 900 °C for 3 hours with a ramp rate of 5 °C min^{-1} under an N_2 atmosphere. After natural cooling, the obtained black powder was denoted as the Co/N/C@Pt$_{0.14}$Co catalyst.

Different amounts of H_2PtCl_6 were applied to control the Pt content in catalysts. By tuning the dosage of H_2PtCl_6 as 78, 117, 156 and 234 μL during precursor preparation, four final catalysts were obtained and named Co/N/C@Pt$_{0.57}$Co, Co/N/C@Pt$_{0.88}$Co, Co/N/C@Pt$_{1.12}$Co and Co/N/C@Pt$_{1.55}$Co.

Physical characterization

The crystal phases of the catalysts were identified by X-ray diffraction (XRD) using a Rigaku Ultima IV diffractometer with Cu Kα X-rays. X-ray photoelectron spectroscopy (XPS) spectra were recorded using a Qtac-100 LEISS setup. The morphology and structure of the catalysts were characterized using high-resolution transmission electron microscopy (HRTEM, FEI Talos F200X) and high-angle annular dark field-scanning transmission electron microscopy (HAADF-STEM, Themis Z). The content of the elements in the catalyst was determined using an inductively coupled plasma-optical emission spectrometer (ICP-OES, Agilent ICP-OES 730).

Electrochemical characterization

Electrochemical measurements were performed using a rotating disk electrode (RDE) system (Pine Instruments). To prepare the working electrode, 4 mg of catalyst was ultrasonically dispersed in 2.0 mL solvent ($V_{\text{isopropyl alcohol}} : V_{\text{water}} = 3:1$). Then 50 μL Nafion (5 wt%) was added to the mixture under ultrasound for 5 minutes to form a uniform catalyst ink. 30 μL catalyst ink was dropped on a disk electrode with an area of 0.196 cm^{-2}, followed by rotary drying at room temperature.

A dried glassy carbon electrode was used as the working electrode (WE), a carbon rod was used as the counter electrode (CE), and an Hg/Hg_2SO_4 electrode (filled with a K_2SO_4-saturated electrolyte) was used as the reference electrode (RE). The potential of Hg/Hg_2SO_4 electrodes was calibrated using Pt foil into H_2-saturated 0.1 M $HClO_4$ as the reversible hydrogen electrode (RHE). All potential values reported in this work are with respect to the reversible hydrogen electrode (RHE).

All the ORR polarization curves were recorded in 0.1 M $HClO_4$ electrolyte. These curves were measured from 0.05–1.1 V with a scan rate at 10 mV in N_2-/O_2-saturated electrolytes, respectively. The accelerated stability tests (ASTs) were evaluated by triangular waves, *i.e.*, cycling the potentials from 0.6 to 1.0 V (scan rate: 50 mV s^{-1}) at 25 °C in the O_2-saturated electrolyte. The kinetic current (I_k) was calculated using the following equation:

$$1/I_a = 1/I_l + 1/I_k$$

where I_a represents apparent current density, I_l represents diffusion limiting current density (current density@0.4 V), and I_k represents kinetics current density.

Results and discussion

It has been widely accepted to prepare M/N/C substrates by pyrolyzing M-doped ZIFs.[41–45] In this work, Co/N/C was synthesized by following a previously reported method.[40] High-resolution transmission electron microscopy (HRTEM) images show that the prepared Co/N/C has a well-defined rhombohedral dodecahedral morphology and no significant nano-

particles can be observed (Fig. S1†). It is noted that a small amount of metallic Co nanoparticles/clusters may exist because the X-ray diffraction (XRD) pattern of Co/N/C shows a small peak at ~44.22°, assigned to metallic Co (JCPDS: 15-0806). Even though, based on the overall energy dispersive spectroscopy (EDX, Fig. S2†) and X-ray photoelectron spectra (XPS, Fig. S3†), it is suggested that the main form of the Co element is the atomically dispersed CoN_x in Co/N/C.

Furthermore, based on Co/N/C, a series of Co/N/C@Pt_xCo catalysts consisting of PtCo NPs on Co/N/C were prepared (x indicates the total Pt/Co ratio, Fig. 1a). ICP-OES was used to analyze the exact contents of Co and Pt in various catalysts (Table S1†). As shown in Fig. 1b, the XRD patterns clearly indicate that the PtCo NPs form particularly when the Pt content is high. Specifically, except Co/N/C@$Pt_{0.14}$Co, other Co/N/C@Pt_xCo samples (including Co/N/C@$Pt_{0.57}$Co, Co/N/C@$Pt_{0.88}$Co and Co/N/C@$Pt_{1.55}$Co) exhibit similar characteristic peaks to a disordered PtCo alloy (JCPDS: 65-8968). Surprisingly, Co/N/C@$Pt_{1.12}$Co shows an ordered (or intermetallic) PtCo characteristic peak (JCPDS: 29-0498). In addition, the characteristic peaks of Co nanoparticles at about 44.22° in Co/N/C disappeared in all the Co/N/C@Pt_xCo samples, which may be due to leaching by formic acid during precursor synthesis and/or the alloying of Co with Pt during pyrolysis.

Fig. 1c–g present the TEM images of Co/N/C@Pt_xCo catalysts with different Pt contents. For catalysts with a low Pt/Co ratio, *e.g.*, Co/N/C@$Pt_{0.14}$Co (Fig. 1c) and Co/N/C@$Pt_{0.57}$Co (Fig. 1d), the distribution of PtCo NPs is not uniform, also being well supported by Fig. S4 and S5.† This may be due to the insufficient Pt source, which is required to form PtCo NPs during the pyrolysis process. It is reported that the preparation of coupled PGM-free@PGM catalysts suffers from batch-to-batch variability, *i.e.*, poor repeatability.[38] This barrier can be attributed to the low Pt content in catalysts, thus forming non-uniform particles. Such a problem requires trade-off between the Pt content and the performance. By increasing the Pt/Co ratio, *e.g.*, Co/N/C@$Pt_{0.88}$Co (Fig. 1e and Fig. S6†) and Co/N/C@$Pt_{1.12}$Co (Fig. 1f and Fig. S7†), the PtCo NPs grow more uniformly. Even though, once the Pt/Co ratio is too high, *e.g.*, Co/N/C@$Pt_{1.55}$Co (Fig. 1g and Fig. S8†), the PtCo NPs grow excessively. In addition, the average particle size increases as the Pt/Co ratio increases (Fig. S9†).

Among all the Co/N/C@Pt_xCo catalysts, the distribution of the PtCo NPs in Co/N/C@$Pt_{0.88}$Co has the best uniformity. The details of this Co/N/C@$Pt_{0.88}$Co catalyst are shown in Fig. 2 and Fig. S10,† well supporting the above discussions. Specifically, Fig. 2h and its inlet clearly show the co-existence of both so-called single atoms (circled with red, Co–N_x) and PtCo nanoparticles in Co/N/C@$Pt_{0.88}$Co. Similarly, other catalysts including Co/N/C@$Pt_{0.57}$Co, Co/N/C@$Pt_{1.12}$Co and Co/N/C@$Pt_{1.55}$Co have comparable features (Fig. S11–S13†). In addition, the existence of Co–N_x moieties can be observed in all the studied catalysts by the deconvolution of Co 2p spectra (Fig. S14–S18†). In short, the above results fully prove the successful construction of the coupled PGM-free@PGM Co/N/C@Pt_xCo catalysts.

To evaluate the effects of the Pt/Co ratio on the ORR performance of Co/N/C@Pt_xCo catalysts, all the samples were

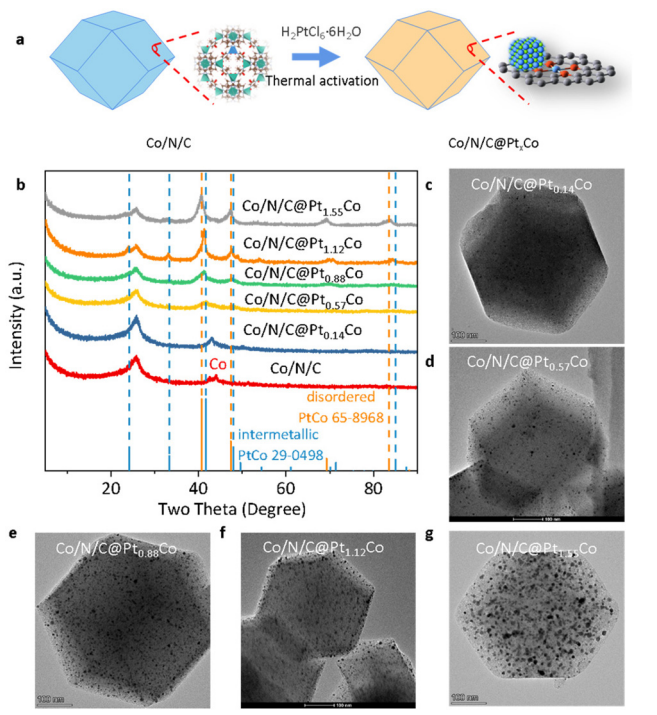

Fig. 1 (a) Schematic of the synthesis of Co/N/C@Pt_xCo. (b) XRD patterns of Co/N/C and various Co/N/C@Pt_xCo samples. TEM images of (c) Co/N/C@$Pt_{0.14}$Co, (d) Co/N/C@$Pt_{0.57}$Co, (e) Co/N/C@$Pt_{0.88}$Co, (f) Co/N/C@$Pt_{1.12}$Co and (g) Co/N/C@$Pt_{1.55}$Co.

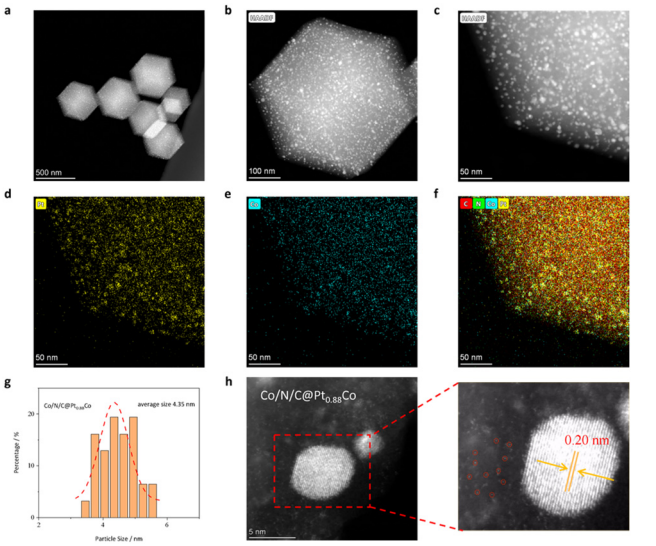

Fig. 2 (a–c) HAADF-STEM images of Co/N/C@$Pt_{0.88}$Co. (d–f) EDX images of Co/N/C@$Pt_{0.88}$Co. (g) Size distribution of PtCo nanoparticles in the Co/N/C@$Pt_{0.88}$Co catalyst. (h) The HAADF-STEM image of the hybrid catalyst and an individual nanoparticle in the Co/N/C@$Pt_{0.88}$Co catalyst.

tested using a rotating disk electrode (RDE) in 0.1 M $HClO_4$ electrolyte. Fig. 3a presents the results of potentiodynamic scanning and demonstrates that the Co/N/C@$Pt_{0.88}$Co catalyst shows the best ORR performance, interestingly, instead of the Co/N/C@$Pt_{1.55}$Co catalyst with the highest Pt content. To be specific, Co/N/C@$Pt_{0.88}$Co shows an onset potential (E_{onset}) of ~1.03 V and a half-wave potential ($E_{1/2}$) of ~0.87 V, which are higher than Co/N/C@$Pt_{0.57}$Co (less Pt) and Co/N/C@$Pt_{1.12}$Co (more Pt) (Fig. 3b and c). All the tests were repeated three times to ensure the repeatability (Fig. S19–S22†), the results of which are consistent with the activity trend as shown in Fig. 3a. The above results illustrate that the Co/N/C@$Pt_{0.88}$Co catalyst exhibits optimal ORR activity in terms of both the half-wave potential and onset potential.

The mass activity (MA) of the catalysts was further calculated and is shown in Fig. 3d. The MA values of Co/N/C@$Pt_{0.88}$Co and Co/N/C@$Pt_{0.57}$Co are much higher than those of other Co/N/C@Pt_xCo catalysts at both 0.9 V and 0.85 V. It was noticed that the MA normalized to the Pt mass of Co/N/C@$Pt_{0.57}$Co is higher than that of Co/N/C@$Pt_{0.88}$Co (Fig. 3d); while Co/N/C@$Pt_{0.88}$Co is higher in MA normalized to the total catalyst mass (Fig. 3e). This is because Co/N/C@$Pt_{0.88}$Co has a slightly higher Pt content and better NP uniformity. Reasonably, the MA of the Co/N/C@$Pt_{0.88}$Co catalyst is 33.33% higher than that of commercial Pt/C (0.16 A mg_{Pt}^{-1} *versus* 0.12 A mg_{Pt}^{-1}) at 0.9 V (Fig. S23†). So far, a volcanic relationship between Pt/Co ratios and ORR activity can be obtained as shown in Fig. 3f.

We further *dig* into the underlying reasons for such a volcanic relationship. The surface chemistry of Co/N/C@Pt_xCo catalysts was analyzed by XPS because electrocatalytic reactions are usually closely related to the surface properties of the catalyst. As shown in Fig. 4a and b, the deconvoluted Pt 4f spectra of Co/N/C@$Pt_{0.88}$Co suggest a negatively shifted binding energy of Pt(0) compared to the benchmark Pt/C, *i.e.*, 71.80 eV for Co/N/C@$Pt_{0.88}$Co *vs.* 72.34 eV for Pt/C, which indicates that Pt gets more electrons in Co/N/C@$Pt_{0.88}$Co and leads to the increased electron cloud density. This further makes the d-band electrons of Pt filled more, leading to the decreased d-band center, which is beneficial for the regulated adsorption and desorption of intermediates during the ORR.[46,47] What should be emphasized is that the excessively decreased d band center will inversely lead to weak adsorption, not conducive to the ORR kinetics.[46,48] This may be one of the reasons for the low ORR activity of Co/N/C@$Pt_{1.12}$Co and Co/N/C@$Pt_{1.55}$Co catalysts (see the Pt 4f XPS spectra of other catalysts in Fig. S24–S26†).

On the other hand, the N 1s XPS spectra were also analyzed, where the peaks located at ~401.1 and ~398.9 eV are assigned to pyrrolic N and pyridinic N, respectively (Fig. 4c and Fig. S27–S30†).[48–50] The contents of pyrrolic and pyridinic N were plotted *vs.* Pt/Co ratios and are shown in Fig. 4d and e.

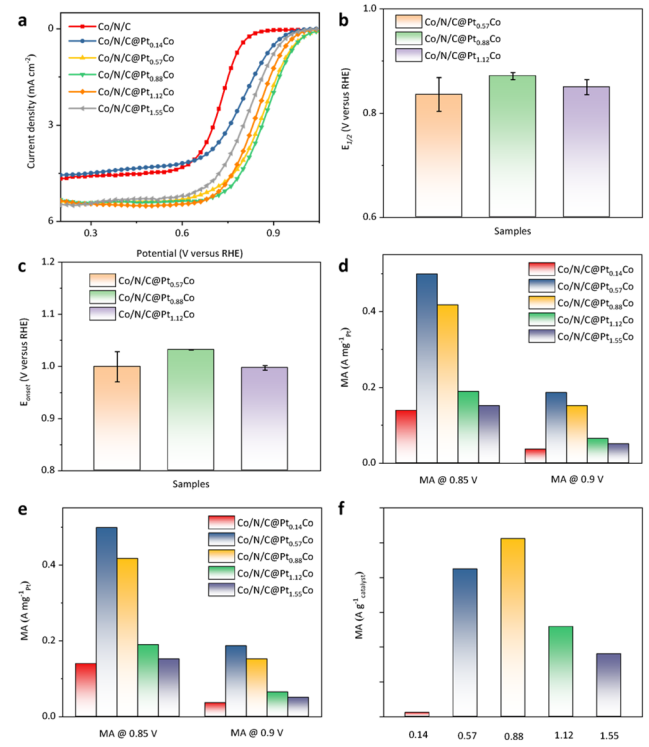

Fig. 3 (a) ORR polarization curves, (b) onset potential (E_{onset}), (c) half-wave potential ($E_{1/2}$), (d) mass activity normalized to Pt mass, (e) mass activity normalized to catalyst mass and (f) the mass activity and Pt/Co ratio (horizontal axis) showing a volcanic-like curve.

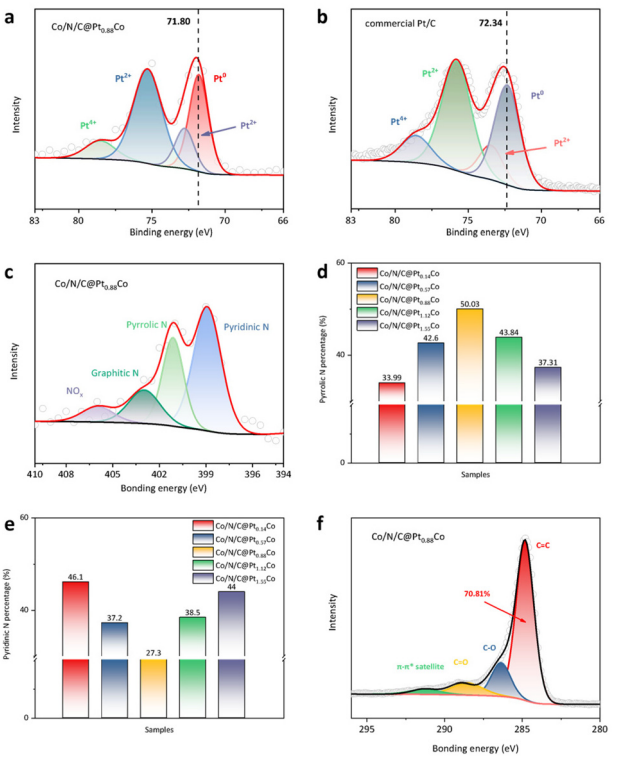

Fig. 4 Pt 4f XPS spectra of (a) Co/N/C@$Pt_{0.88}$Co and (b) commercial Pt/C. (c) N 1s XPS spectra of Co/N/C@$Pt_{0.88}$Co. The content of (d) pyrrolic N and (e) pyridinic N of various Co/N/C@Pt_xCo catalysts. (f) C 1s XPS spectra of Co/N/C@$Pt_{0.88}$Co.

Interestingly, the concentration of pyrrolic N first increases and then decreases with the increased Pt/Co ratio (Fig. 4d), while pyridinic N shows an opposite trend (Fig. 4e). In short, the N dopants show a (inverted) volcanic relationship as well. In addition to pyrrolic and pyridinic N, the contents of graphitic N and oxidized N have little change (Table S2†). Combined with the volcanic relationship in ORR MA, it is concluded that an appropriate Pt content in Co/N/C@Pt$_x$Co catalysts is required to regulate the formation of pyrrolic N and pyridinic N; the pyrrolic and pyridinic N likely play an important role in facilitating the ORR on Co/N/C@Pt$_x$Co catalysts.[51–53]

The above results show that the coupled Co/N/C@Pt$_x$Co catalysts with low Pt content can indeed improve the ORR performance, and the overall ORR performance has a volcanic relationship with the Pt/Co ratio in the catalysts. By optimizing the amount of Pt source, the performance of the catalyst can be optimized *via* tuning particle size/distribution and pyrrolic/pyridinic N.[53–57] In addition to activity, the stability of catalysts were also studied. As shown in Fig. 5a, after 30 000-cycle potentiodynamic scanning between 0.6 and 1.1 V in the O_2-saturated 0.1 M $HClO_4$ electrolyte, the polarization curve of Co/N/C@Pt$_{0.88}$Co has little change, whose $E_{1/2}$ loss is only 10 mV, lower than those of Co/N/C@Pt$_{0.14}$Co (11 mV, Fig. 5b) and Co/N/C@Pt$_{1.55}$Co (28 mV, Fig. 5c). In particular, all these three Co/N/C@Pt$_x$Co catalysts have much smaller activity loss than commercial Pt (99 mV, Fig. 5d) under the same testing protocol.

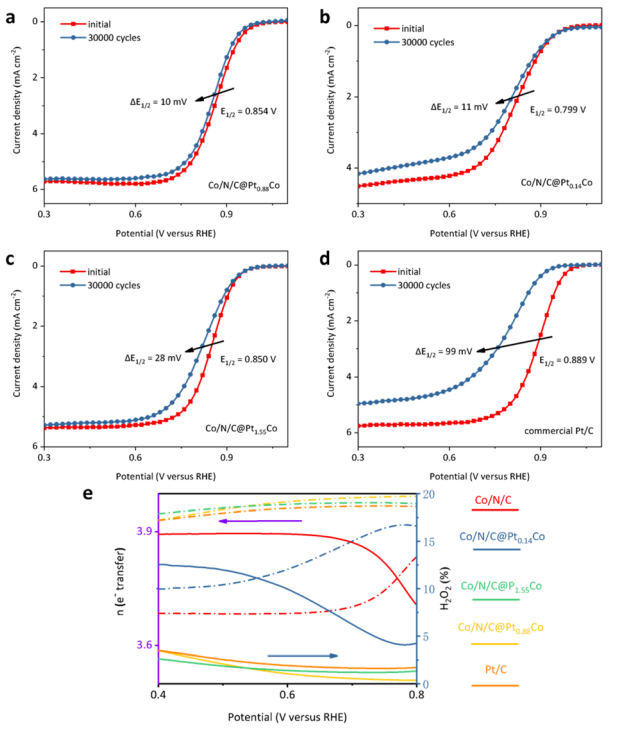

Fig. 5 ORR polarization curves of (a) Co/N/C@Pt$_{0.88}$Co, (b) Co/N/C@Pt$_{0.14}$Co, (c) Co/N/C@Pt$_{1.55}$Co and (d) Pt/C before and after 30 000-cycle ASTs. (e) Electron transfer number (left axis) and hydrogen peroxide production rate (right axis) of various catalysts.

The enhanced stability can be due to the higher graphitization degree of catalysts. As shown in Fig. 4f, Fig. S31–S36 and Table S3,† the graphitic C content of Co/N/C@Pt$_{0.88}$Co is the highest among all the samples. On the other hand, the strong metal–support interaction (SMSI) between the PGM moiety (PtCo nanoparticles) and the PGM-free moiety (Co/N/C support) could be another reason for the improved stability.[49,58] Given the optimal N dopants in Co/N/C@Pt$_{0.88}$Co, its SMSI can be well regulated and thus leads to better stability than other samples.[57,59] Meanwhile, the peroxide intermediate during the ORR and its derivative free radicals have been widely reported to have a bad effect on the stability of ORR catalysts. As shown in Fig. 5e, in the presence of a small amount of Pt, even as low as ~1 wt% (*i.e.*, Co/N/C@Pt$_{0.14}$Co catalyst), peroxide can be substantially suppressed.

Conclusions

In conclusion, the optimization of the emerging and advanced coupled Co/N/C@Pt$_x$Co catalysts is performed in this work by adjusting the amount of Pt source. The results demonstrate a (inverted) volcanic relationship between the Pt/Co ratio in the catalysts and their physical and electrochemical properties, including the NP uniformity, N dopant contents, ORR mass activity, and stability. Among the catalysts, Co/N/C@Pt$_{0.88}$Co achieves a higher mass activity that exceeds that of commercial Pt/C by 33% (0.16 A mg_{Pt}^{-1} *vs.* 0.12 A mg_{Pt}^{-1}) and also much better stability. These results indicate that a moderate Pt/Co ratio is indispensable in Co/N/C@Pt$_x$Co catalysts. This work not only synthesizes a series of Co/N/C@Pt$_x$Co catalysts but also clarifies their structure–activity relationships, which would be helpful in designing advanced PGM-free@PGM electrocatalysts for the ORR and beyond.

Author contributions

Yangdong Zhou: conceptualization, methodology, investigation, and writing – original draft. Junda Chen: investigation and software. Zhiyin Huang: investigation, software, and funding acquisition. Yuqin Peng: investigation and software. Lixin Xing: writing – review & editing. Chunmei Tang: writing – review & editing. Ning Wang: writing – review & editing. Ling Meng: writing – review & editing. Mingjie Wu: conceptualization, writing – review & editing. Lei Du: conceptualization, writing – review & editing, funding acquisition, and supervision. Siyu Ye: writing – review & editing, funding acquisition, and supervision.

Conflicts of interest

There are no conflicts to declare.

Acknowledgements

This work was supported by the National Natural Science Foundation of China (22250710133), the Outstanding Youth Project of Natural Science Foundation of Guangdong Province (2022B1515020020), the Guangdong Basic and Applied Basic Research Foundation (2022B1515120079), the Science and Technology Projects in Guangzhou (2024A03J0308), the Graduate "Basic innovation" Project of Guangzhou University (2022GDJC-M10), and the Guangdong Engineering Technology Research Center for Hydrogen Energy and Fuel Cells.

Notes and references

1 Y. Zhou, N. Wang, L. Xing, X. Zhang, R. Zhong, Y. Peng, Y. Chen, S. Ye, X. Xie and L. Du, *Chem Catal.*, 2023, **3**, 100484.
2 L. Du, Y. Shao, J. Sun, G. Yin, J. Liu and Y. Wang, *Nano Energy*, 2016, **29**, 314–322.
3 L. Du, L. Xing, G. Zhang, M. Dubois and S. Sun, *Small Methods*, 2020, **4**, 2000016.
4 X. Zou, S. G. Chen, Q. M. Wang, X. Y. Gao, J. Li, J. Li, L. Li, W. Ding and Z. D. Wei, *Nanoscale*, 2019, **11**, 20115–20122.
5 S. Katayama, Characterization and analysis of the new generation Mirai catalysts (in Japanese), **https://fc-cubic-event.jp/wp-sympo/wp-content/uploads/2022/05/bb54e72f169-dae5e5c564288d6405f16.pdf**.
6 W. J. Zeng, C. Wang, Q. Q. Yan, P. Yin, L. Tong and H. W. Liang, *Nat. Commun.*, 2022, **13**, 7654.
7 X. Tian, X. Zhao, Y. Q. Su, L. Wang, H. Wang, D. Dang, B. Chi, H. Liu, E. J. M. Hensen, X. W. D. Lou and B. Y. Xia, *Science*, 2019, **366**, 850–856.
8 J. P. Owejan, J. E. Owejan and W. Gu, *J. Electrochem. Soc.*, 2013, **160**, F824–F833.
9 A. Kongkanand and M. F. Mathias, *J. Phys. Chem. Lett.*, 2016, **7**, 1127–1137.
10 V. Prabhakaran, G. Wang, J. Parrondo and V. Ramani, *J. Electrochem. Soc.*, 2016, **163**, F1611–F1617.
11 J. Huang, Z. Li and J. Zhang, *Front. Energy*, 2017, **11**, 334–364.
12 S. Shen, X. Cheng, C. Wang, X. Yan, C. Ke, J. Yin and J. Zhang, *Phys. Chem. Chem. Phys.*, 2017, **19**, 26221–26229.
13 R. K. Ahluwalia, X. Wang, J. K. Peng, N. N. Kariuki, D. J. Myers, S. Rasouli, P. J. Ferreira, Z. Yang, A. Martinez-Bonastre, D. Fongalland and J. Sharman, *J. Electrochem. Soc.*, 2018, **165**, F3316–F3327.
14 R. Singh, P. C. Sui, K. H. Wong, E. Kjeang, S. Knights and N. Djilali, *J. Electrochem. Soc.*, 2018, **165**, F3328–F3336.
15 X. Cheng, C. Wang, G. Wei, X. Yan, S. Shen, C. Ke, F. Zhu and J. Zhang, *J. Electrochem. Soc.*, 2019, **166**, F1055–F1061.
16 L. Pan, S. Ott, F. Dionigi and P. Strasser, *Curr. Opin. Electrochem.*, 2019, **18**, 61–71.
17 T. Schuler, A. Chowdhury, A. T. Freiberg, B. Sneed, F. B. Spingler, M. C. Tucker, K. L. More, C. J. Radke and A. Z. Weber, *J. Electrochem. Soc.*, 2019, **166**, F3020–F3031.
18 C. Wang, X. Cheng, X. Yan, S. Shen, C. Ke, G. Wei and J. Zhang, *J. Electrochem. Soc.*, 2019, **166**, F239–F245.
19 Z. Zheng, L. Luo, F. Zhu, X. Cheng, F. Yang, S. Shen, G. Wei and J. Zhang, *Electrochim. Acta*, 2019, **323**, 134751.
20 R. L. Borup, A. Kusoglu, K. C. Neyerlin, R. Mukundan, R. K. Ahluwalia, D. A. Cullen, K. L. More, A. Z. Weber and D. J. Myers, *Curr. Opin. Electrochem.*, 2020, **21**, 192–200.
21 S. Ott, A. Orfanidi, H. Schmies, B. Anke, H. N. Nong, J. Hubner, U. Gernert, M. Gliech, M. Lerch and P. Strasser, *Nat. Mater.*, 2020, **19**, 77–85.
22 Z. Zheng, F. Yang, C. Lin, F. Zhu, S. Shen, G. Wei and J. Zhang, *J. Power Sources*, 2020, **451**, 227729.
23 X. Cheng, G. Wei, C. Wang, S. Shen and J. Zhang, *Int. J. Heat Mass Transfer*, 2021, **164**, 120549.
24 L. Du, V. Prabhakaran, X. Xie, S. Park, Y. Wang and Y. Shao, *Adv. Mater.*, 2021, **33**, e1908232.
25 X. Yang, W. Sun, J. Chen, Y. Gao, R. Zhang, Q. Luo, T. Lyu and L. Du, *J. Mater. Sci. Technol.*, 2024, **173**, 100–106.
26 F. Y. Zhou, Y. Ruan, M. Z. Zhu, X. P. Gao, W. X. Guo, X. K. Liu, W. Y. Wang, M. Chen, G. Wu, T. Yao, H. Zhou and Y. Wu, *Small*, 2023, **19**, 2302328.
27 W. H. Lai, L. Zhang, Z. Yan, W. Hua, S. Indris, Y. Lei, H. Liu, Y. X. Wang, Z. Hu, H. K. Liu, S. Chou, G. Wang and S. X. Dou, *Nano Lett.*, 2021, **21**, 7970–7978.
28 S. Yin, Y. N. Yan, L. Chen, N. Cheng, X. Cheng, R. Huang, H. Huang, B. Zhang, Y. X. Jiang and S. G. Sun, *ACS Nano*, 2023, **18**, 551–559.
29 J. Chen, J. Dong, J. Huo, C. Li, L. Du, Z. Cui and S. Liao, *Small*, 2023, **19**, e2301337.
30 W. Guo, X. Gao, M. Zhu, C. Xu, X. Zhu, X. Zhao, R. Sun, Z. Xue, J. Song, L. Tian, J. Xu, W. Chen, Y. Lin, Y. Li, H. Zhou and Y. Wu, *Energy Environ. Sci.*, 2023, **16**, 148–156.
31 Y. Zeng, J. Liang, B. Li, H. Yu, B. Zhang, K. S. Reeves, D. A. Cullen, X. Li, D. Su, G. Wang, S. Zhong, H. Xu, N. Macauley and G. Wu, *ACS Catal.*, 2023, **13**, 11871–11882.
32 F. Xiao, Q. Wang, G.-L. Xu, X. Qin, I. Hwang, C.-J. Sun, M. Liu, W. Hua, H.-w. Wu, S. Zhu, J.-C. Li, J.-G. Wang, Y. Zhu, D. Wu, Z. Wei, M. Gu, K. Amine and M. Shao, *Nat. Catal.*, 2022, **5**, 503–512.
33 Y. Xiong, Y. Yang, F. J. DiSalvo and H. D. Abruna, *ACS Nano*, 2020, **14**, 13069–13080.
34 L. Huang, Y. Q. Su, R. Qi, D. Dang, Y. Qin, S. Xi, S. Zaman, B. You, S. Ding and B. Y. Xia, *Angew. Chem., Int. Ed.*, 2021, **60**, 25530–25537.
35 P. Guo, Y. Xia, B. Liu, M. Ma, L. Shen, Y. Dai, Z. Zhang, Z. Zhao, Y. Zhang, L. Zhao and Z. Wang, *ACS Appl. Mater. Interfaces*, 2022, **14**, 53819–53827.
36 L. Chong, J. Wen, J. Kubal, F. G. Sen, J. Zou, J. Greeley, M. Chan, H. Barkholtz, W. Ding and D. J. Liu, *Science*, 2018, **362**, 1276–1281.
37 L. Chong, H. Zhou, J. Kubal, Q. Tang, J. Wen, Z. Yang, I. D. Bloom, D. Abraham, H. Zhu, J. Zou and W. Ding, *Chem Catal.*, 2023, **3**, 100541.
38 D-J. Liu, H. Xu and L. Chong, *Argonne National Laboratory*, 2020, **https://www.hydrogen.energy.gov/docs/hydrogenprogram-libraries/pdfs/review20/fc174_liu_2020_p.pdf?Status=Master**.

39 Y. Luo, K. Li, Y. T. Chen, J. Z. Feng, L. K. Wang, Y. G. Jiang, L. J. Li, G. Yu and J. Feng, *Adv. Mater.*, 2023, **35**, 2300624–2300638.
40 W. Sun, L. Du, Q. Tan, J. Zhou, Y. Hu, C. Du, Y. Gao and G. Yin, *ACS Appl. Mater. Interfaces*, 2019, **11**, 41258–41266.
41 L. Sun, Y. Qin and Y. Yin, *J. Power Sources*, 2023, **562**, 232758.
42 R. Wang, P. Zhang, Y. Wang, Y. Wang, K. Zaghib and Z. Zhou, *Prog. Nat. Sci.*, 2020, **30**, 855–860.
43 L. Shang, H. Yu, X. Huang, T. Bian, R. Shi, Y. Zhao, G. I. N. Waterhouse, L. Z. Wu, C. H. Tung and T. Zhang, *Adv. Mater.*, 2015, **28**, 1668–1674.
44 Y. Ye, F. Cai, H. Li, H. Wu, G. Wang, Y. Li, S. Miao, S. Xie, R. Si, J. Wang and X. Bao, *Nano Energy*, 2017, **38**, 281–289.
45 B. Chi, L. Zhang, X. Yang, Y. Zeng, Y. Deng, M. Liu, J. Huo, C. Li, X. Zhang, X. Shi, Y. Shao, L. Gu, L. Zheng, Z. Cui, S. Liao and G. Wu, *ACS Catal.*, 2023, **13**, 4221–4230.
46 J. Greeley, I. E. Stephens, A. S. Bondarenko, T. P. Johansson, H. A. Hansen, T. F. Jaramillo, J. Rossmeisl, I. Chorkendorff and J. K. Norskov, *Nat. Chem.*, 2009, **1**, 552–556.
47 J. R. Kitchin, J. K. Norskov, M. A. Barteau and J. G. Chen, *J. Chem. Phys.*, 2004, **120**, 10240–10246.
48 J. Lai, S. Chen, X. Liu, X. Yan, Z. Qin, L. Xie, Z. Lin, Z. Cai, Y. Zhao, H.-L. Wang, Y. Huang and Q. Li, *ACS Catal.*, 2023, **13**, 11996–12006.
49 W. Yu, H. Huang, Y. Qin, D. Zhang, Y. Zhang, K. Liu, Y. Zhang, J. Lai and L. Wang, *Adv. Energy Mater.*, 2022, **12**, 2200110–2200117.
50 X. X. Wang, S. Hwang, Y. T. Pan, K. Chen, Y. H. He, S. Karakalos, H. G. Zhang, J. S. Spendelow, D. Su and G. Wu, *Nano Lett.*, 2018, **18**, 4163–4171.
51 L. F. Li, G. K. Han, Y. D. Wen, Y. X. Liu, R. Xiao, W. Zhang, F. P. Kong, L. Du, Y. L. Ma, P. J. Zuo, C. Y. Du and G. P. Yin, *Fuel*, 2023, **345**, 128199.
52 S. Y. Chen, T. Luo, X. Q. Li, K. J. Chen, J. W. Fu, K. Liu, C. Cai, Q. Y. Wang, H. M. Li, Y. Chen, C. Ma, L. Zhu, Y. R. Lu, T. S. Chan, M. S. Zhu, E. Cortes and M. Liu, *J. Am. Chem. Soc.*, 2022, **144**, 14505–14516.
53 N. Zhang, T. P. Zhou, M. L. Chen, H. Feng, R. L. Yuan, C. A. Zhong, W. S. Yan, Y. C. Tian, X. J. Wu, W. S. Chu, C. Z. Wu and Y. Xie, *Energy Environ. Sci.*, 2020, **13**, 111–118.
54 L. Yan, L. Y. Xie, X. L. Wu, M. Y. Qian, J. R. Chen, Y. J. Zhong and Y. Hu, *Carbon Energy*, 2021, **3**, 856–865.
55 P. P. Sun, Z. L. Qiao, S. T. Wang, D. Y. Li, X. R. Liu, Q. H. Zhang, L. R. Zheng, Z. B. Zhuang and D. P. Cao, *Angew. Chem., Int. Ed.*, 2023, **62**, e202216041.
56 L. J. Yuan, B. Liu, L. X. Shen, Y. K. Dai, Q. Li, C. Liu, W. Gong, X. L. Sui and Z. B. Wang, *Adv. Mater.*, 2023, **35**, 2305945–2305955.
57 X. Hu, S. Chen, L. Chen, Y. Tian, S. Yao, Z. Lu, X. Zhang and Z. Zhou, *J. Am. Chem. Soc.*, 2022, **144**, 18144–18152.
58 Z. Qiao, C. Wang, C. Li, Y. Zeng, S. Hwang, B. Li, S. Karakalos, J. Park, A. J. Kropf, E. C. Wegener, Q. Gong, H. Xu, G. Wang, D. J. Myers, J. Xie, J. S. Spendelow and G. Wu, *Energy Environ. Sci.*, 2021, **14**, 4948–4960.
59 Y. Ha, B. Fei, X. Yan, H. Xu, Z. Chen, L. Shi, M. Fu, W. Xu and R. Wu, *Adv. Energy Mater.*, 2020, **10**, 2002592–2002600.